

A Versatile Polymeric Precursor to High-Performance Silicon Composite Anode for Lithium-Ion Batteries

Kai Yang, Zhihao Yu, Changcheng Yu, Min Zhu, Luyi Yang, Haibiao Chen,* and Feng Pan*

Silicon is a promising anode material for lithium-ion batteries due to its very high theoretical capacity. Herein, a Si/SiO_x@C composite anode is prepared from a polymeric precursor, and the performance of the anode is optimized by controlling the composition of the polymeric precursor. The precursor is produced by cross-linking divinyl benzene (DVB) and polymethylhydrosiloxane (PMHS). Silicon nanoparticles are formed from the precursor via a molten-salt reduction process, and a conductive SiO_x@C matrix is produced through a subsequent pyrolysis process. As the ratio between DVB and PMHS is adjusted to 2:1, the specific capacity and rate performances of the resulting Si/SiO_x@C composite reach the optima. Both the composition and the microstructure of the composite are affected by the composition of the precursor, and, in turn, they determine the performance of the composite anode.

1. Introduction

Lithium-ion batteries (LIBs) become the most popular power source in portable electronics and electric vehicles, and graphite is normally used as the anode material in commercial LIBs. Graphite reaches its theoretical capacity (372 mAh g⁻¹) when lithium ions insert between the layers of graphite and form LiC₆.^[1] There is currently an increasing demand for high-performance anode materials with high specific capacity, power density, and cyclic stability. Various novel anode materials have been explored, and silicon is a promising candidate due to several advantages: high theoretical capacity (3579 mAh g⁻¹),^[2] low-voltage plateau, abundant reserve, and low cost. However, the use of silicon as a practical anode material is still not realistic due to the low intrinsic electric conductivity and severe volume change (>300%) of silicon during the lithiation/delithiation processes, which causes severe capacity fade upon cycling.^[1,3]

Tremendous efforts have been devoted to address the instability issue of silicon anodes, and common strategies include 1) reducing the dimension of silicon by preparing nanowires,^[4] nanofibers,^[5] and nanoparticles^[6] to reduce internal stress upon


volume change; 2) introducing porosity,^[7] which could provide space to buffer the volume change and shorten the lithium-ion diffusion distance; 3) the use of novel binders^[8] to ensure constant contact while accommodating the volume change; and 4) wrapping silicon nanoparticles in a flexible and conductive carbon shell^[9] or matrix^[10] to form a Si/C composite.^[11] Among these strategies, Si/C composite seems to be a promising and cost-effective solution. A robust and continuous carbon shell or matrix provides ability to enhance the electric conductivity as well as to buffer the volume change of silicon and thus enhance the cyclic stability of the anode. The carbon shell or matrix can also hold the fractured silicon particles, transfer electrons and

lithium ions quickly, and form a stable solid electrolyte interphase (SEI) layer.

Si-based compounds are also explored as alternative lithium storage materials in addition to elemental Si. As an anode material, silicon oxycarbide (SiOC)^[12] can offer a reversible capacity of 600–800 mAh g⁻¹ and shows a great cyclic stability with some modifications. Similar to the Si/C composites, supplementing SiOC with a free carbon phase (SiO_x@C)^[13] can introduce a continuous matrix, which offers excellent electrical conductivity as well as flexibility to buffer the volume change. To take advantage of both Si/C and SiO_x@C, researchers have tried to embed silicon particles in a matrix of SiO_x@C through different ways.^[13a,14] Different strategies have been demonstrated to optimize the electrochemical performance of Si/C composite anode materials, including tuning of the composition,^[9b,10d,13b,15] morphology, and structure.^[10c,14b,16] In many earlier works, the silicon particles and the carbon-containing matrix are from separate sources. In research works, silicon nanoparticles were typically purchased from a chemical supplier and coated, embedded, or wrapped using a carbon precursor. To commercialize these technologies, the cost to produce the silicon nanoparticles should be considered. In addition, as the carbon precursor is introduced to pre-existing silicon nanoparticles, it often requires a carefully designed and precisely controlled process to form a homogeneous composite.

In a polysiloxane, Si and C are homogeneously distributed at the molecular level. It is possible to produce silicon nanoparticles and a carbon-rich matrix from a single source, such as a polysiloxane precursor.^[14c] A unique benefit using a polymer precursor is the flexibility of tuning the composition of the precursor at the

K. Yang, Z. Yu, C. Yu, M. Zhu, L. Yang, Prof. H. Chen, Prof. F. Pan
School of Advanced Materials
Peking University Shenzhen Graduate School
Shenzhen 518055, P. R. China
E-mail: chenhb@pkusz.edu.cn; panfeng@pkusz.edu.cn

 The ORCID identification number(s) for the author(s) of this article can be found under <https://doi.org/10.1002/ente.201900239>.

DOI: 10.1002/ente.201900239

molecular level. In this work, we produced a Si/SiO_x@C composite with a homogeneous distribution of silicon nanoparticles in a continuous carbon-containing matrix from a polymeric precursor using a low-temperature molten-salt reduction process and subsequent pyrolysis. By adjusting the composition of the precursor, we analyzed the effect on the composition and the structure of the Si/SiO_x@C composite and the resulting electrochemical performance. For a versatile control on the composition of the precursor, divinyl benzene (DVB) as a C source was used to cross-link polymethylhydrosiloxane (PMHS) to produce a polymer precursor, of which the composition was controlled by the ratio between the two reactants. As the composition of the polymeric precursor changed, the composition and the structure of the final Si/SiO_x@C composite were affected. By analyzing the electrochemical performance of the Si/SiO_x@C anode, an optimal composition of the precursor can be identified. This approach enables a process for preparing Si/C-type composite anode with a versatile control on the composition and the structure. In addition, the costs of DVB and PMHS are relatively low, and the process will be potentially viable for commercialization.

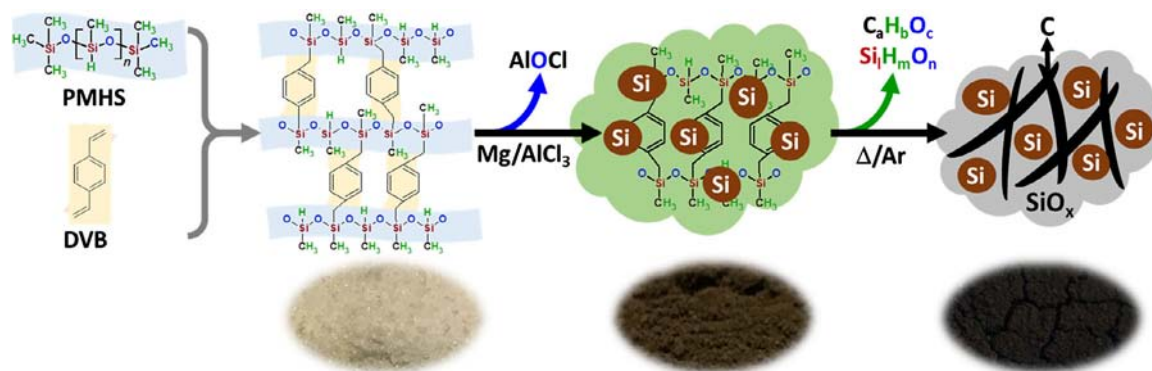
2. Results and Discussion

The overall synthesis process of the Si/SiO_x@C composite is schematically shown in **Scheme 1**. DVB was used as a cross-linker to cure PMHS into a solid silicone elastomer, which was used as the polymeric precursor. The polymeric precursor was labelled as P3-1, P2-1, P1-1, P1-2, and P1-3, respectively, according to the DVB to PMHS ratio. PMHS contains a hydride group (—SiH)^[17] in every repeating unit, and it can be used to cure vinyl-terminated polysiloxane by addition polymerization. DVB contains two vinyl groups^[18] available for addition polymerization. The C=C bonds in DVB react with the active Si—H in PMHS with a Pt-containing catalyst, as verified by the Fourier-transform infrared (FTIR) results shown in **Figure 1a** and **Figure S1**, Supporting Information. Characteristic signals of vinyl group^[19] vibration in the DVB polymer are present at 901 and 988 cm⁻¹, which become diminished in the cross-linked product. Similarly, the intensity of the peak at 2163 cm⁻¹ from the Si—H groups^[17] decreased after cross-linking. The cross-linked product was heated at 360 °C to further harden the polymer and to remove unstable residues. After the heat

treatment at 360 °C, the polymer remained clear in color, and it can be easily ground into powders. The polymer powders were then subjected to the low-temperature molten-salt magnesiothermic reduction to produce elemental Si. The molten AlCl₃ salt not only serves as a liquid bed to enable the homogeneous mixing of the reactants, but it also participates in the reaction.^[14c,20] The color of the reduced product was dark brown as shown in **Figure S2**, Supporting Information, indicating the formation of a new phase. After pyrolysis of the reduced product at 900 °C, the final product turned black, which suggested carbonization of the organic phase. The final product was labelled as CS3-1, CS2-1, CS1-1, CS1-2, or CS1-3, respectively, according to the precursor.

The materials after the molten-salt reduction were examined by X-ray diffraction (XRD), and the results are shown in **Figure 1b**. Peaks at 28.5°, 47.4°, 56.2°, 69.3°, and 76.6° can be ascribed to the (111), (220), (311), (400), and (331) planes of cubic Si, respectively.^[15] The XRD results confirmed that the elemental Si was successfully reduced from the polymer precursor. The XRD of the materials after subsequent pyrolysis confirmed that the elemental Si remained after pyrolysis. Using the Scherrer equation, an average diameter of the Si crystallite in the final products was calculated from the broadening of the (111) peak and summarized in **Table S1**, Supporting Information. The average diameter was between 20 and 40 nm, and it increased as the Si content in the precursor increased. The presence of graphitic phase in the materials cannot be identified by XRD. For further confirmation of the phases, Raman spectra of the final products were obtained, and the spectrum for CS2-1 is shown in **Figure 1c**. The strong peaks located around 505.3 and 930.6 cm⁻¹ match the peak positions of crystalline Si.^[13a] In addition, two peaks located around 1330.8 and 1589.3 cm⁻¹ were identified as the characteristic D-band and G-band of graphitic carbon, respectively.^[13a] The ratio between the intensities of G-band and D-band, i.e., I_G/I_D of CS2-1, was calculated to be 1.46, which is higher than that of the other two composites as shown in **Figure S3** and **Table S2**, Supporting Information, suggesting that CS2-1 has a higher degree of graphitization and potentially a better electrical conductivity.

The elemental contents of Si and C in the cross-linked products as functions of the ratio between DVB and PHMS were calculated and plotted in **Figure 1d**. As DVB does not contain any Si and is rich in carbon, the C content decreases and the



Scheme 1. Overall synthesis process of Si/SiO_x@C anode material.

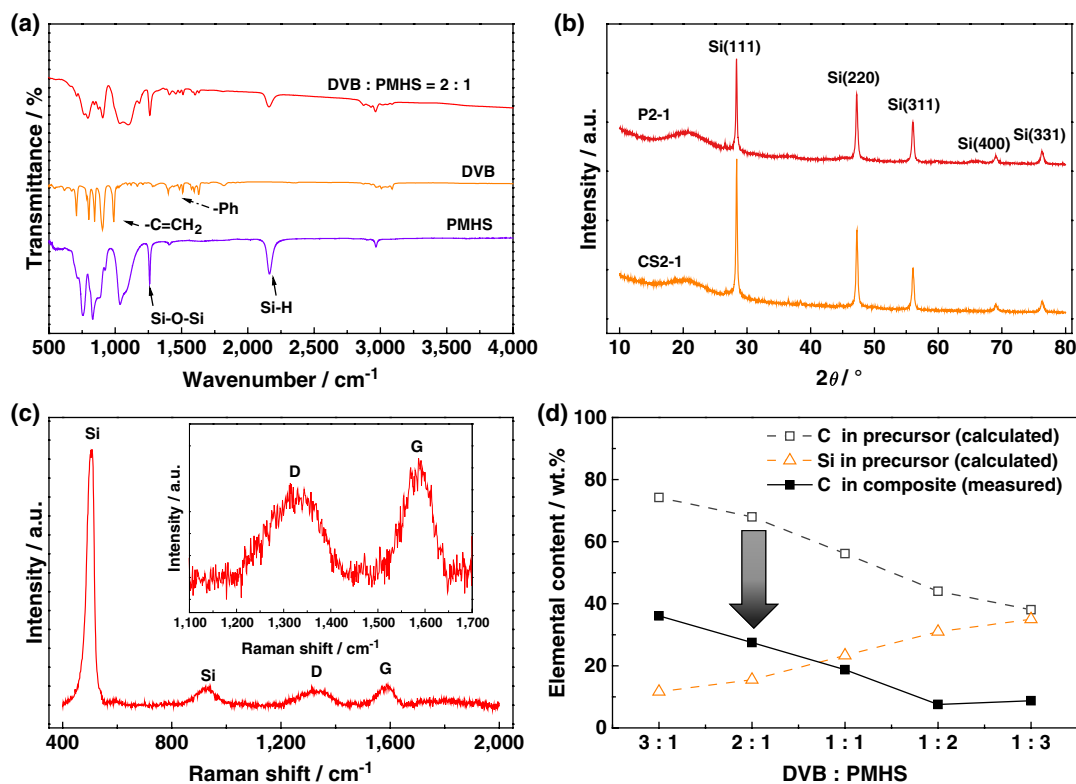


Figure 1. a) FTIR spectra of PMHS, DVB, and the cross-linked polymer. b) XRD patterns of the reduced product P2-1 and CS2-1. c) Raman spectra of the Si/SiO_x@C composite CS2-1 (inset) enlarged region of 1100–1700 cm⁻¹, showing D and G bands. d) Calculated C and Si contents in the precursors and the measured C content in the Si/SiO_x@C composites.

Si content increases as the DVB/PMHS ratio decreases. The C content in the final Si/SiO_x@C composite was measured using the element analyzer and plotted as a function of the DVB/PMHS ratio. The trends of C content as a function of the DVB/PMHS ratio are similar in the precursor and in the final Si/SiO_x@C composite, although the actual measured C content was consistently lower than that calculated in the precursor. There are two major reasons for causing the decrease in the C content from the precursor to the final Si/SiO_x@C composite. First, the conversion of a polymer precursor to an inorganic composite by pyrolysis involves decomposition of the precursor and evaporation of small molecule volatiles, causing the loss of carbon. Second, the C content in the final Si/SiO_x@C composite measured by an element analyzer is actually only the content of the free carbon phase that can be oxidized at 1200 °C, and there might be more C bound to Si, which cannot be easily oxidized and measured. Nevertheless, the matching trends between the calculated C content in the precursor and the semiquantitative measurement confirm that the composition of the Si/SiO_x@C composite can be varied by simply adjusting the DVB/PMHS ratio. Among the five ratios, the electrochemical performance reached the optimum in the ratio where DVB/PMHS equals 2 (Table S4 and S5, and Figure S9, Supporting Information). Therefore, the following discussion is focused on the three ratios, which are 3, 2, and 1, corresponding to precursors P3-1, P2-1, and P1-1, and composites CS3-1, CS2-1, and CS1-1, respectively.

The chemical composition of the Si/SiO_x@C composites near the surface was further analyzed using X-ray photoelectron spectroscopy (XPS), and the results are shown in Figure 2 and Figure S4, Supporting Information. In the survey spectrum of CS2-1, a typical Si 2p peak at around 102 eV, Si 2s peak at around 153 eV, C 1s peak at around 284 eV, and O 1s peak at around 532 eV can be identified. Please note that the strong O peak can partially originate from the surface adsorbed molecules and may not reflect the actual composition of the material. High-resolution Si 2p spectrum of CS2-1 can be further deconvoluted into three peaks, corresponding to the Si—Si bonds at around 99.4 eV, the Si—C bonds at around 101.5 eV, and the Si—O bonds at around 102.8 eV, respectively.^[21] The C 1s spectrum can be deconvoluted into three peaks, corresponding to the C—Si bonds at around 283.7 eV, the C—C bonds at around 284.8 eV, and the C=O bonds at around 285.7 eV, respectively.^[22] The Si 2p and C 1s spectra confirmed the presence of elemental Si, free carbon, Si—C bond, and Si—O bond in the composite. The elemental contents of the three composites were derived using the XPS data and shown in Figure 2d. Note that the XPS analysis is surface-sensitive, and it is only used as a semi-quantitative indicator of the bulk composition. The C content decreased and the Si content increased in the order of CS3-1, CS2-1, and CS1-1. The trend is similar to that previously shown in Figure 1d. As a supplementary analysis, the free carbon content was also calculated from the thermogravimetric analysis (TGA) curves (Figure S5, Supporting Information), and the trend

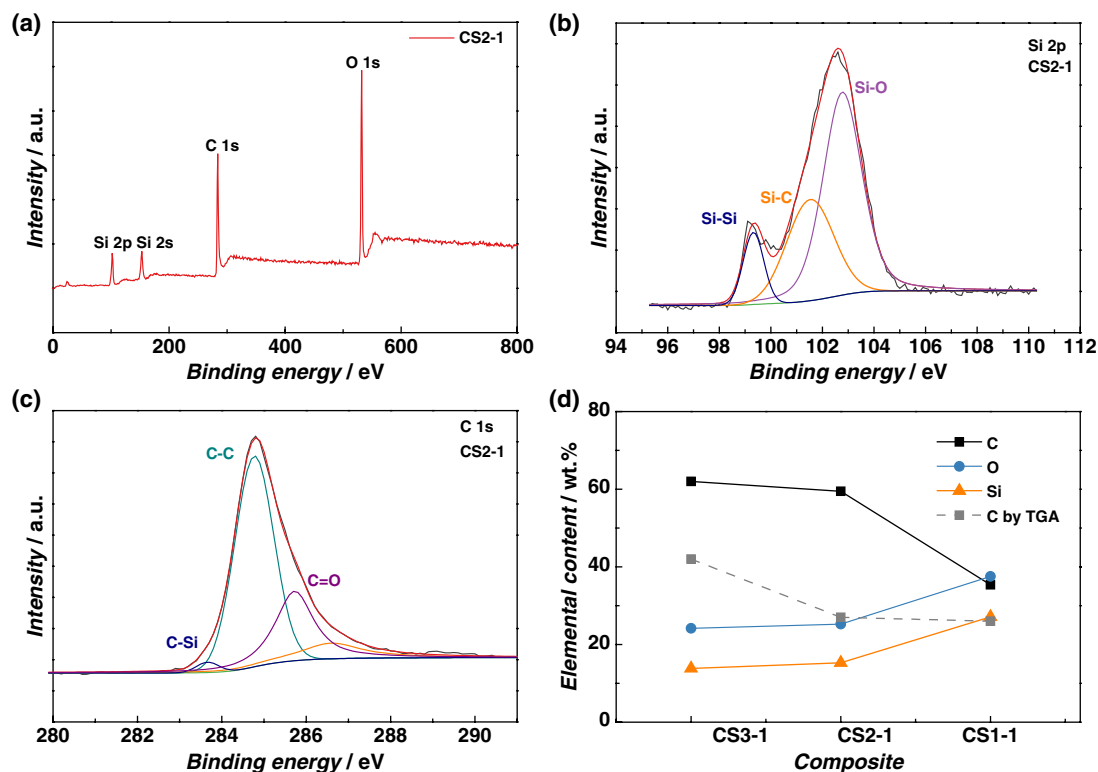


Figure 2. XPS analysis of the Si/SiO_x@C composites: a) survey spectrum of CS2-1, b) high-resolution Si 2p spectrum of CS2-1, c) high-resolution C 1s spectrum of CS2-1, and d) elemental contents of C, Si, and O of the composites by XPS, and the C content by TGA for comparison.

is similar. However, the TGA analysis is based only on the weight change, and it cannot distinguish whether the weight loss is caused by carbon oxidation or by evaporation of the absorbed species. Therefore, it is difficult to correlate the result of TGA and that of the elemental analyzer quantitatively.

The structure of the Si/SiO_x@C composites was observed using scanning electron microscopy (SEM), and the images are shown in **Figure 3**. There is no significant difference in the structure between the materials. The agglomerates of CS3-1 appear to be larger and consist of micrometer-sized particles (**Figure 3a**), whereas CS2-1 and CS1-1 (**Figure 3b,c**) consist of finer and more spherical particles. The different morphologies between the materials might be partially related to the different compositions of the precursors. Energy dispersive X-ray spectroscopy (EDS) elemental mapping confirmed that the Si, O, and C elements are uniformly distributed at the microscopic level across the particles (**Figure 3d**, and **Figure S6 and S7**, Supporting Information). However, a quantitative EDS analysis of the composition did not yield consistent results. By nitrogen physisorption, the specific pore volume of CS2-1 was measured to be 2.39 cm³ g⁻¹, and the pore-size distribution and nitrogen adsorption/desorption isotherm are shown in **Figure S8 and S9**, Supporting Information. The morphology of the material appeared to be loose agglomerates of finer particles. Most of the pore volume is contributed by the macropores, which are likely the interstitial space between the primary particles. For optimal performance, a higher packing density with a low specific pore volume is preferred. Transmission electron microscopy (TEM) confirmed the presence

of crystallites embedded in an amorphous matrix in all the Si/SiO_x@C composites. As shown in **Figure 3e**, the fringe spacing within the crystallite is 0.31 nm, which matches the *d*-spacing of the (111) atomic planes of crystalline Si. The average particle size of the Si crystallites was estimated to be in the range of 20–40 nm, which matches the XRD calculation.

The electrochemical performance of the composite as an anode material for LIB was evaluated in coin cells. The cyclic voltammetry (CV) curves of cells with fresh composite anodes are shown in **Figure 4a** and **Figure S10a,b**, Supporting Information. There is a gradual change in the shape of the CV curve for the first five cycles. There was a broad cathodic peak in the first cycle, which should be related to the formation of the SEI layer accompanied by the decomposition of the electrolyte. This peak disappeared in the following cycles, suggesting that a stable SEI layer has formed. In the charging branch, two peaks at 0.36 and 0.52 V typically identifying the lithium-ion extraction in Si gradually intensified from cycle to cycle. The gradual intensification of these two peaks is a sign of an activation process of the anode. Also, there is a peak at around 0.18 V, which started to appear in the cathodic branch and gradually intensified, and this peak has been previously related to the transformation of an amorphous Li_xSi phase.^[23] The CV measurement confirms that metallic silicon is the major active component for lithium storage in the Si/SiO_x@C composites.

The results of galvanostatic charging/discharging measurements are shown in **Figure 4b**, and **Figure S10c and S10d**, Supporting Information. In the first discharging (lithiation)

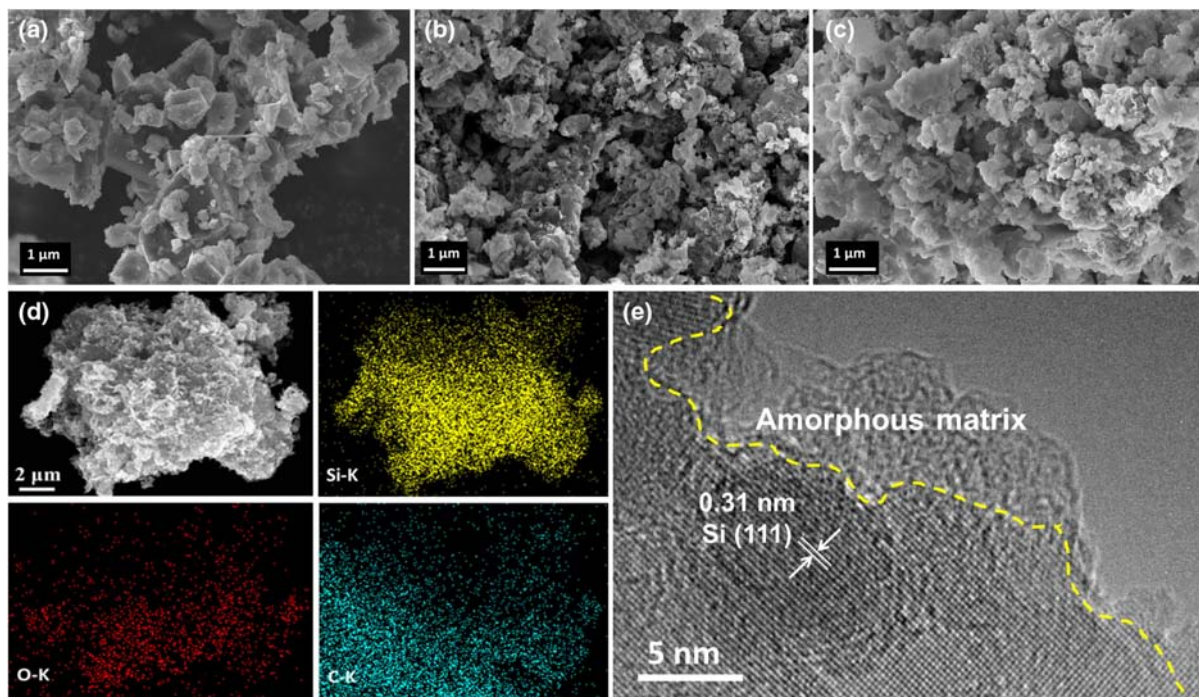


Figure 3. SEM images of a) CS3-1, b) CS2-1, and c) CS1-1. d) EDS elemental mapping of CS2-1. e) TEM image of CS2-1.

curve, the relatively slower voltage drop from 1.5 to 0.3 V could be related to the reduction of electrolyte to form an SEI layer and the reduction of some SiO_x to Si.^[13b] Most of the capacity observed in this region cannot be recovered via lithium extraction in the subsequent charging (delithiation) process. As a result, there is a significant loss in the capacity in the first charging (delithiation) curve and a low initial coulombic efficiency (ICE) for the first cycle. Table S3, Supporting Information, summarizes the initial capacity and ICE of the composite anode materials, which are 1216 mAh g^{-1} and 59% for CS3-1, 2396 mAh g^{-1} and 66% for CS2-1, 1460 mAh g^{-1} and 74% for CS1-1, 1432 mAh g^{-1} and 74% for CS1-2, and 1423 mAh g^{-1} and 70% for CS1-3, respectively. CS2-1 exhibited the highest initial capacity, and CS1-1 showed the highest ICE. Overall, CS2-1 showed the highest reversible capacity in the first cycle. The ICE appeared to be increasing as the C content decreased. As the structure of an amorphous carbon tends to be fractal, an SEI layer with a large surface area will form and consume more lithium when the C content is high. Although the Si content was assumed to be increasing from CS2-1 to CS1-3, the reversible capacity decreased unexpectedly. It seems that either the change in the microstructure or the content of inactive Si such as that in SiO_x has a considerable effect on the reversible lithium storage capacity as the composition changed. Another look at the XRD data of CS1-1 as shown in Figure S11, Supporting Information, finds several low-intensity peaks from unknown substances. The peaks at around 36° and 70° can be from 6H-SiC. Therefore, it is likely that there are SiC and other inactive by-products from the synthesis process, and these by-products cause the lower specific capacity of CS1-1. Among all five tested materials, CS2-1 appeared to be the optimal anode for LIBs.

Measuring the capacity at higher charging/discharging rates can provide information on charge transfer rates in the anode. The rate capacities of the composite anodes are presented in Figure 4c and Figure S12a, Supporting Information, at various current densities from 0.1 to 0.2, 0.4, 0.8, 1, 1.5, 2, and 5 A g^{-1} , and finally back to 0.1 A g^{-1} . Detailed rate performance results are summarized in Table S4, Supporting Information. CS2-1 showed clearly the highest capacity at all rates, and the discharging capacity changed from 1239 to 1226, 1174, 1063, 982, 885, 820, and 626 mAh g^{-1} and finally came back to 1119 mAh g^{-1} at the corresponding forth-mentioned rates. Bulk Si anode materials often showed low capacity values at high rates because of the low intrinsic electrical conductivity. Carbon matrix especially graphitic carbon could generally improve the conductivity. In addition, the $\text{SiO}_x@\text{C}$ matrix provided a constant electrical contact between the silicon nanoparticles and the electrolyte even when the volume change was significant, thus facilitating fast charge transfer at high charging/discharging rates. As all other processing conditions are the same for all the materials, it appeared that an optimal composite structure of $\text{Si/SiO}_x@\text{C}$ was achieved by controlling the composition of the precursor. Figure 4d and Figure S12b, Supporting Information, show the cycling performance of composite anodes in the voltage range of 0.01–2.0 V at a constant current density of 0.4 A g^{-1} . Each cell was activated at a current density of 0.1 A g^{-1} in the first five cycles to ensure that the formation of a stable SEI was complete. Table S5, Supporting Information, summarizes the capacity retention rates of the $\text{Si/SiO}_x@\text{C}$ composite anodes. After 100 cycles, 60% of the initial capacity remained for CS3-1, 72% for CS2-1, and 80% for CS1-1. Rapid capacity decay was a common issue for Si anodes, and here, the SiO_x and carbon matrix

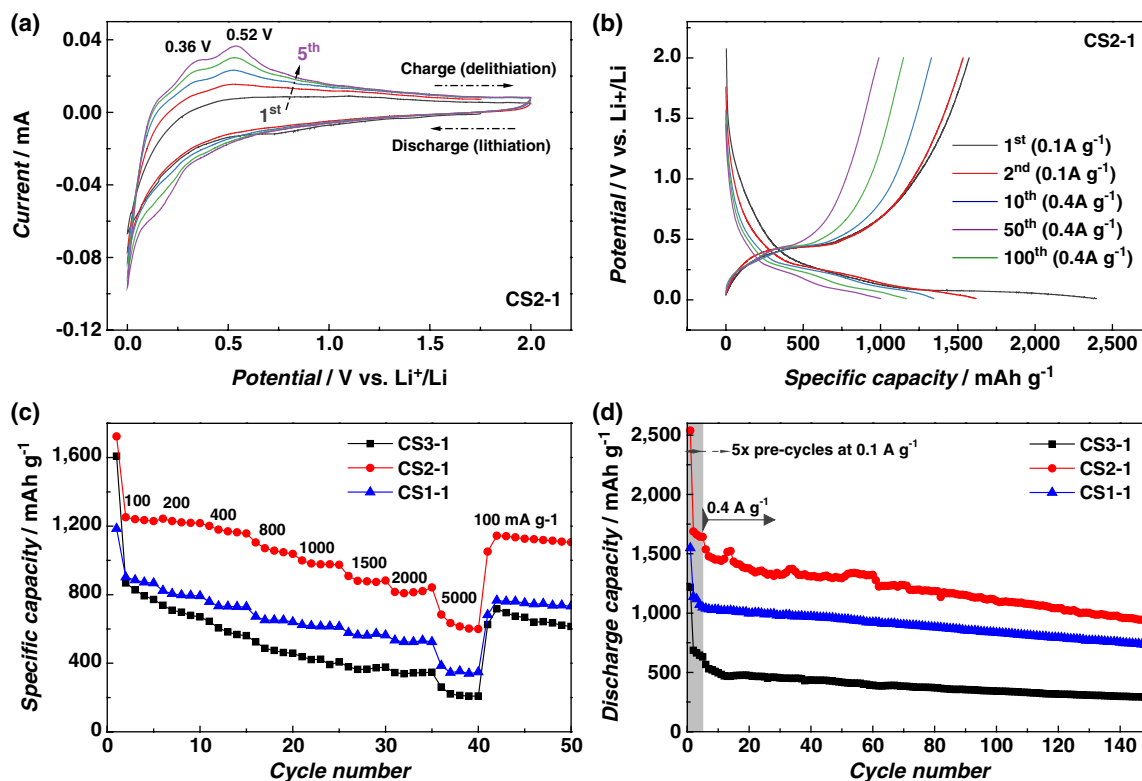


Figure 4. Electrochemical measurement of the Si/SiO_x@C composites: a) CV curves of CS2-1 at a scan rate of 0.5 mV s⁻¹, b) charging/discharging profiles of the CS2-1 during the 1st, 2nd, 10th, 50th, and 100th cycles, c) rate performance at various current densities, the voltage range is 0.01–2.0 V versus Li⁺/Li, and d) cycling performance at 0.4 A g⁻¹, each cell was activated for five cycles at 0.1 A g⁻¹ before cycling.

provided mechanical support to buffer the volume change of Si. However, a higher content of SiO_x and carbon matrix did not necessarily lead to better stability. As shown in Figure 3, the structure of CS3-1 is different from that of CS2-1 or CS1-1. It is likely that the structure of CS3-1 itself is not mechanically

stable in comparison with CS2-1 or CS1-1 and tends to collapse during the charging and discharging processes. To verify this hypothesis, we used SEM to observe the electrodes after cycling.

After the cycling test, the anodes were removed from the cells, and the surface of the anodes was examined. As shown in Figure 5,

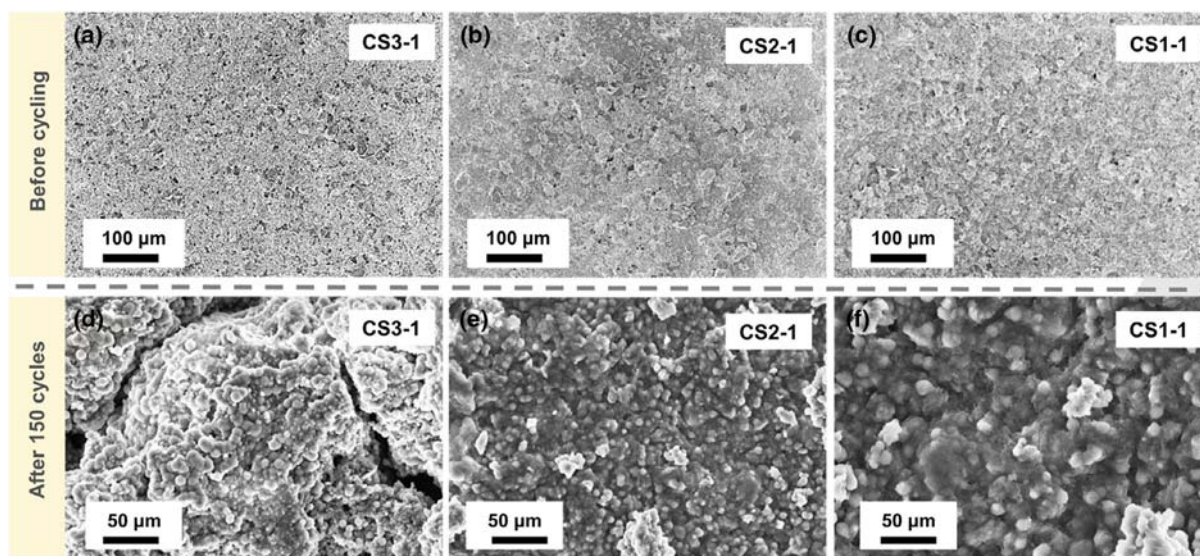


Figure 5. SEM images of the electrode surface before and after 150 cycles: a–c) surface of the electrode before cycling and d–f) surface of the electrode after 150 cycles. Each cell was activated at a current density of 0.1 A g⁻¹ for five precycles and then cycled at 0.4 A g⁻¹.

there were no obvious cracks or delamination on the surface of all three fresh anodes. After 150 cycles, different morphologies were observed in the anodes. Cracks and delamination were observed in the CS3-1 anode. The surfaces of CS2-1 and CS1-1 did not change noticeably. Detailed SEM images (Figure S13–S15, Supporting Information) show that there were continuous SEI layers covering the surface of the anodes after cycling for CS2-1 and CS1-1. The SEM observation is consistent with the better cycling stability of CS2-1 and CS1-1 in comparison with CS3-1. It appeared that a higher content of carbon in the precursor did not necessarily lead to a better stability, and the structure of the final composite needs to be considered as a factor. In a Si composite anode, the electrolyte would reduce to form an SEI layer during the first cycle. After repeated lithium insertion and extraction, Si particles suffer cycles of volume change and may pulverize when the internal stress becomes too high. If the matrix is fragile, the anode itself can fracture, and the electrolyte can infiltrate the crack and form a new SEI layer on the fresh surface. This causes irreversible consumption of the lithium ions and reduces the coulombic efficiency (Figure S16a, Supporting Information). The structure of CS3-1 appeared to be fragile as shown in Figure 3a. In contrast, in Si/SiO_x@C with an optimal composite structure, Si nanoparticles were embedded in a robust matrix of SiO_x@C (Figure S16b, Supporting Information). The continuous and flexible matrix is mechanically robust, so it provides a “buffer zone” to accommodate the volume change in the Si particles. A continuous SEI layer can constantly enclose the whole composite particle during the cycles. Even if the Si nanoparticles fracture, the fragments still remain inside the matrix and the original SEI layer and continue to be active for reversible lithium storage.

3. Conclusions

In summary, via a low-temperature molten-salt magnesiothermic reduction method, a Si/SiO_x@C composite was synthesized, where Si particles were embedded in the SiO_x/C matrix. By tuning the ratio between the reactants for producing the polymeric precursor, a Si/SiO_x@C composition (CS2-1) with optimal electrochemical performance was obtained. It is proposed that the unique structure and composition of CS2-1 enable high rate performance and cycling stability without compromising the high capacity of Si. On the one hand, the graphitic carbon network provides a highly conductive network. Therefore, the rate performance had been greatly improved (626 mAh g⁻¹ at a high current density of 5 A g⁻¹). On the other hand, a continuous SiO_x and carbon matrix could serve as a mechanically stable network to buffer the volume change caused by Si particles, resulting in the formation of stable SEI layers; hence, the cycling stability was improved (specific capacity retention of 72% after 100 cycles at a current density of 400 mA g⁻¹). The method to control the composition and the structure of the composite via polymerization of various siloxane precursors was a promising and effective way to design new Si/SiO_x@C anode composite materials for optimal performance. For future work, polysiloxanes at potentially lower costs, such as moisture-cured silicones or recycled silicones, can be used to produce high-performance Si/C anodes at even lower costs.

4. Experimental Section

Synthesis of Si/SiO_x@C Composite: In a typical procedure, DVB (Sigma–Aldrich) and PMHS (Sigma–Aldrich) in five different mass ratios (3:1, 2:1, 1:1, 1:2, and 1:3 with a total mass of 10 g) were mixed with a Pt catalyst (15 μL, platinum (0)-1, 3-divinyl-1, 1, 3, 3-tetramethyldisiloxane complex solution in xylene, Sigma–Aldrich) in a disposable cup, and the mixture was manually stirred for 10 min. The mixture was set overnight, followed by heat treatment at 360 °C in a tube furnace for 100 min under argon flow to ensure complete cross-linking. After cooling down to room temperature, the polymer was collected and ground into powders. Precursor (1 g), magnesium powder (1 g, Aladdin), and AlCl₃ (8 g, Aladdin) were mixed and loaded into a stainless steel hydrothermal reactor, which was heated to 220 °C for 10 h in an oven to reduce Si from the precursor. After cooling down to room temperature, the product was collected and washed with 0.2 M hydrochloric acid and deionized water to remove the by-products and remaining AlCl₃. The resulting sample was dried in an oven at 80 °C overnight. Then, it was heated to 900 °C at a ramp rate of 5 °C min⁻¹ in a tube furnace and held at the peak temperature for 4 h under argon flow. After cooling down to room temperature, the product was collected.

Characterization: FTIR spectra of all precursors were collected using a Perkin Elmer Frontier spectrometer to evaluate the degree of polymerization. A Bruker D8 Advance diffractometer (Cu Kα radiation, λ = 1.5405 Å) was used to analyze the crystalline phases in all composites. Raman spectra were collected to identify metallic silicon and graphitic carbon using an iHR320 spectrometer with a Synapse charge-coupled device (CCD) detector (Horiba Instruments Inc.). The content of free carbon in the composite was analyzed using a vario EL cube analyzer (Elementar Analysensysteme GmbH). TGA in dry air was used to confirm the free carbon content using a Mettler-Toledo TGA/DSC-1 system. The microstructures of the composites were imaged using the Zeiss Supra 55 SEM. The TEM was performed to identify silicone crystallites and to analyze the structure of the matrix using an FEI Tecnai G2. The XPS was collected to analyze the surface composition of the composites using an ESCALAB 250XL X-ray photoelectron spectrometer. Nitrogen physisorption analysis was carried out on a Micromeritics ASAP 2020 to characterize the pore structure of the optimized Si/SiO_x@C material. The specific pore volume was obtained by the Barrett–Joyner–Halenda (BJH) model, and the pore-size distribution (PSD) was derived by a density functional theory (DFT) model based on the nitrogen adsorption data.

Electrochemical Performance: The electrochemical performance of the Si/SiO_x@C composite as an anode material in an LIB was evaluated using a half-cell configuration in 2032-type coin cells. The Si/SiO_x@C composite material was mixed with acetylene black and 1.5 wt% poly(acrylic acid) (PAA, Mw = 3 000 000, Aldrich) solution in a weight ratio of Si/SiO_x@C:acetylene black:PAA = 70:15:15. The resulting slurry was casted onto a copper foil and then dried at 80 °C in a vacuum oven overnight. The average mass loading of active material in the electrode was about 1.2 mg cm⁻². The coated copper foil was punched into disks to produce the working electrodes. Half cells were assembled in an argon-filled glovebox with Si/SiO_x@C as the working electrode, a lithium foil (Aldrich) as the counter electrode, a Celgard 2400 microporous membrane as the separator, and 1 M LiPF₆ in ethylene carbonate and diethyl carbonate (EC:DEC = 1:1 by volume) with 5 wt% fluoroethylenecarbonate as the electrolyte. Galvanostatic charging and discharging were measured using a Neware battery testing system (Neware, China) in the voltage range of 0.01–2.0 V at room temperature. For the cycling tests, all cells were run for five precycles at 0.1 A g⁻¹ to activate the electrode and then run at 0.4 A g⁻¹ in the subsequent cycles. The CV measurements were made on a CHI660 electrochemical workstation (Shanghai Chenhua Instrument Co. Ltd., China). The CV measurements were carried out in the voltage range of 0–2.0 V using a scan rate of 0.2 mV s⁻¹.

Supporting Information

Supporting Information is available from the Wiley Online Library or from the author.

Acknowledgements

K.Y. and Z.Y. contributed equally to this work. This research was financially supported by the Shenzhen Science and Technology Research Grant No. JCYJ20170818085823773, the Guangdong Key-lab Project No. 2017B0303010130, and the National Materials Genome Project 2016YFB0700600.

Conflict of Interest

The authors declare no conflict of interest.

Keywords

composition, lithium-ion batteries, polymer precursors, silicon composite anodes

Received: February 21, 2019

Revised: April 3, 2019

Published online: May 13, 2019

- [1] J. Lu, Z. Chen, F. Pan, Y. Cui, K. Amine, *Electrochem. Energy Rev.* **2018**, *1*, 35.
- [2] Y. Kubota, M. C. S. Escaño, H. Nakanishi, H. Kasai, *J. Appl. Phys.* **2007**, *102*, 053704.
- [3] a) J. Wang, T. Xu, X. Huang, H. Li, T. Ma, *RSC Adv.* **2016**, *6*, 87778; b) X. Zuo, J. Zhu, P. Müller-Buschbaum, Y.-J. Cheng, *Nano Energy* **2017**, *31*, 113; c) K. Feng, M. Li, W. Liu, A. G. Kashkooli, X. Xiao, M. Cai, Z. Chen, *Small* **2018**, *14*, 1702737.
- [4] C. K. Chan, H. Peng, G. Liu, K. McIlwrath, X. F. Zhang, R. A. Huggins, Y. Cui, *Nat. Nanotechnol.* **2007**, *3*, 31.
- [5] Z. Favors, H. H. Bay, Z. Mutlu, K. Ahmed, R. Ionescu, R. Ye, M. Ozkan, C. S. Ozkan, *Sci. Rep.* **2015**, *5*, 8246.
- [6] a) L. Hu, H. Wu, S. S. Hong, L. Cui, J. R. McDonough, S. Bohy, Y. Cui, *Chem. Commun.* **2011**, *47*, 367; b) S. Xun, X. Song, L. Wang, M. E. Grass, Z. Liu, V. S. Battaglia, G. Liu, *J. Electrochem. Soc.* **2011**, *158*, A1260; c) M. Wu, J. E. C. Sabisch, X. Song, A. M. Minor, V. S. Battaglia, G. Liu, *Nano Lett.* **2013**, *13*, 5397.
- [7] a) H. Kim, B. Han, J. Choo, J. Cho, *Angew. Chem., Int. Ed.* **2008**, *47*, 10151; b) J. Cho, *J. Mater. Chem.* **2010**, *20*, 4009; c) D. Chen, X. Mei, G. Ji, M. Lu, J. Xie, J. Lu, J. Y. Lee, *Angew. Chem., Int. Ed.* **2012**, *51*, 2409.
- [8] a) A. Magasinski, B. Zdyrko, I. Kovalenko, B. Hertzberg, R. Burtovyy, C. F. Huebner, T. F. Fuller, I. Luzinov, G. Yushin, *ACS Appl. Mater. Interfaces* **2010**, *2*, 3004; b) B. Koo, H. Kim, Y. Cho, K. T. Lee, N.-S. Choi, J. Cho, *Angew. Chem., Int. Ed.* **2012**, *51*, 8762;
- c) D. Liu, Y. Zhao, R. Tan, L.-L. Tian, Y. Liu, H. Chen, F. Pan, *Nano Energy* **2017**, *36*, 206; d) Y. Zhao, L. Yang, Y. Zuo, Z. Song, F. Liu, K. Li, F. Pan, *ACS Appl. Mater. Interfaces* **2018**, *10*, 27795.
- [9] a) N. Liu, H. Wu, M. T. McDowell, Y. Yao, C. Wang, Y. Cui, *Nano Lett.* **2012**, *12*, 3315; b) L. Xue, G. Xu, Y. Li, S. Li, K. Fu, Q. Shi, X. Zhang, *ACS Appl. Mater. Interfaces* **2013**, *5*, 21; c) Z. Lu, N. Liu, H.-W. Lee, J. Zhao, W. Li, Y. Li, Y. Cui, *ACS Nano* **2015**, *9*, 2540; d) B. Jiang, S. Zeng, H. Wang, D. Liu, J. Qian, Y. Cao, H. Yang, X. Ai, *ACS Appl. Mater. Interfaces* **2016**, *8*, 31611.
- [10] a) J. Luo, X. Zhao, J. Wu, H. D. Jang, H. H. Kung, J. Huang, *J. Phys. Chem. Lett.* **2012**, *3*, 1824; b) X. Zhou, Y.-X. Yin, L.-J. Wan, Y.-G. Guo, *Adv. Energy Mater.* **2012**, *2*, 1086; c) W. Sun, R. Hu, H. Liu, M. Zeng, L. Yang, H. Wang, M. Zhu, *J. Power Sources* **2014**, *268*, 610; d) J. Kim, C. Oh, C. Chae, D.-H. Yeom, J. Choi, N. Kim, E.-S. Oh, J. K. Lee, *J. Mater. Chem. A* **2015**, *3*, 18684.
- [11] a) H. Zhang, X. Qin, J. Wu, Y.-B. He, H. Du, B. Li, F. Kang, *J. Mater. Chem. A* **2015**, *3*, 7112; b) G. Liang, X. Qin, J. Zou, L. Luo, Y. Wang, M. Wu, H. Zhu, G. Chen, F. Kang, B. Li, *Carbon* **2018**, *127*, 424.
- [12] J. Yang, Y. Takeda, N. Imanishi, C. Capiglia, J. Y. Xie, O. Yamamoto, *Solid State Ionics* **2002**, *152–153*, 125.
- [13] a) Y.-S. Hu, R. Demir-Cakan, M.-M. Titirici, J.-O. Müller, R. Schlögl, M. Antonietti, J. Maier, *Angew. Chem., Int. Ed.* **2008**, *47*, 1645; b) D. Wang, M. Gao, H. Pan, J. Wang, Y. Liu, *J. Power Sources* **2014**, *256*, 190.
- [14] a) S. J. Lee, H. J. Kim, T. H. Hwang, S. Choi, S. H. Park, E. Deniz, D. S. Jung, J. W. Choi, *Nano Lett.* **2017**, *17*, 1870; b) J. Zhang, J. Gu, H. He, M. Li, *J. Solid State Electrochem.* **2017**, *21*, 2259; c) M. Zhu, J. Yang, Z. Yu, H. Chen, F. Pan, *J. Mater. Chem. A* **2017**, *5*, 7026.
- [15] R. Zhang, Y. Du, D. Li, D. Shen, J. Yang, Z. Guo, H. K. Liu, A. A. Elzatahry, D. Zhao, *Adv. Mater.* **2014**, *26*, 6749.
- [16] S. Guo, X. Hu, Y. Hou, Z. Wen, *ACS Appl. Mater. Interfaces* **2017**, *9*, 42084.
- [17] M. Wójcik-Bania, A. Łącz, A. Nyczyk-Malinowska, M. Hasik, *Polymer* **2017**, *130*, 170.
- [18] a) H. Yang, J. Irudayaraj, M. M. Paradkar, *Food Chem.* **2005**, *93*, 25; b) O. O. Sonibare, T. Haeger, S. F. Foley, *Energy* **2010**, *35*, 5347.
- [19] B. Podko cielna, M. Sobiesiak, *J. Therm. Anal. Calorim.* **2017**, *127*, 625.
- [20] N. Lin, Y. Han, J. Zhou, K. Zhang, T. Xu, Y. Zhu, Y. Qian, *Energy Environ. Sci.* **2015**, *8*, 3187.
- [21] Z. Wen, G. Lu, S. Cui, H. Kim, S. Ci, J. Jiang, P. T. Hurley, J. Chen, *Nanoscale* **2014**, *6*, 342.
- [22] M. Halim, C. Hudaya, A. Y. Kim, J. K. Lee, *J. Mater. Chem. A* **2016**, *4*, 2651.
- [23] W. Ren, Y. Wang, Z. Zhang, Q. Tan, Z. Zhong, F. Su, *J. Mater. Chem. A* **2016**, *4*, 552.